

Path-Tracking Control of an Autonomous 4WS4WD Electric Vehicle Using Its Natural Feedback Loops

Ramprasad Potluri and Arun Kant Singh

Abstract—A four-wheel steering four-wheel drive electric vehicle has a steering motor and a driving motor for each wheel, for a total of eight motors. Almost all of the existing path-tracking controllers for this vehicle are designed by viewing the mathematical model of the vehicle as the system of equations $\dot{x} = f(x, u)$, $y = h(x, u)$, and are mathematically sophisticated. In contrast, this brief presents a block diagrammatic representation of the model, and exploits the natural feedback loops revealed through this representation to develop two novel and useful results: 1) a mathematically simpler path-tracking controller that promises to be easier to tune and 2) a constraint on the wheel accelerations that helps constrain the wheel slips to a desired value. Simulations illustrate this solution.

Index Terms—Active wheel, autonomous corner module, disturbance observer (DOB), electric corner module, four-wheel steering four-wheel drive (4WS4WD), input-to-state stability (ISS), path-tracking control (PTC).

I. INTRODUCTION

FOUR-WHEEL steering four-wheel drive (4WS4WD) electric vehicles (EVs) have an independent steering motor and an independent driving motor for each wheel. The driving motor may be an in-wheel motor. These vehicles combine the advantages of 4WD capability, such as superior traction/braking force distribution and superior acceleration [1], with that of 4WS capability, such as maneuverability and handling [2].

4WS4WD EVs have received attention from the industry [3]–[5] as well as the academic community. Research on 4WS4WD EVs has focused on the problems of tire-force distribution [1], [6], development of prototypes and laboratory scale testbeds [7], path-tracking control (PTC) [8]–[12], fault-tolerant PTC [13], and fault-tolerant control of the motors [14]. This brief restricts itself to developing a simple solution to the problem of PTC. Future work can attempt to introduce fault-tolerance into this solution.

The existing works on the PTC of a 4WS4WD EV treat its mathematical model as the system of equations $\dot{x} = f(x, u)$, $y = h(x, u)$, and apply various mathematically sophisticated control and estimation techniques on these equations. Peng [8] and Peng *et al.* [9] use linearization, singular perturbation, robust bounded control, algebraic Riccati equations, and linear matrix inequalities. Li *et al.* [14] use Lyapunov stability theory to develop fault-tolerant controllers for the driving

Manuscript received June 26, 2014; accepted January 4, 2015. Manuscript received in final form January 19, 2015. This work was supported by the Department of Science and Technology under Project SR/S3/EECE/0076/2012. Recommended by Associate Editor J. Lu.

The authors are with the Department of Electrical Engineering, IIT Kanpur, Kanpur 208016, India (e-mail: potluri@iitk.ac.in; arunkant@iitk.ac.in).

Digital Object Identifier 10.1109/TCST.2015.2395994

and steering motors. Yang *et al.* [13] and Chen *et al.* [15] use the linearized version of the model presented in [8] and [9]. The control in [13] combines a so-called *linear-quadratic-based progressive accommodation technique* and a control-Lyapunov function method. The controller in [15] is built through a multiobjective optimization approach using a linear matrix inequality that combines quadratic stabilization with constraints on inputs. Ploeg *et al.* [11], [12] decompose the problem of PTC of the vehicle into one where each wheel subsystem needs to track its own reference path, assign a model of the form $\dot{x} = f(x, u)$ and $y = h(x, u)$ to each wheel subsystem, design controllers involving feedback linearization, and use Kalman filters to estimate the states of the wheel subsystems from the sensed states of the vehicle body.

Controllers that do not use such sophisticated math are possible, as shown in [16] and [17]. The latter work shows that an examination of the natural feedback loops in the vehicle model helps develop a PTC solution that does not use any state observers, and has only three proportional-integral-derivative (PID) controllers to tune. The individual motor control systems (MCSs) can be tuned independently of the PTC system; so they are not counted among the controllers to tune. Thanks to an invertible decoupling matrix, each of these PID controllers needs to be tuned assuming a nominal single input single output plant of the form $1/s$. Industry values simple-to-tune controllers even over those mathematically sophisticated controllers that assure superior performance and robustness, when these latter controllers are difficult to tune [18], [19].

While the block diagrammatic representation of a model may seem natural and easy, its power is frequently overlooked in many control problems. The contribution of the line of research started in [16] and [17], and continued in this brief is the block diagrammatic representation of the vehicle model along with two novel and useful insights derived from this representation. The first insight helps develop a mathematically simple path-tracking controller, which additionally promises to be simple to tune in practice, using a model that has been treated by earlier authors only as $\dot{x} = f(x, u)$, $y = h(x, u)$ and based on which mathematically sophisticated controllers were developed. The second insight helps develop a novel constraint on the wheel accelerations, respecting which helps constrain the wheel slips.

This brief presents simulation results that help examine the performance of the PTC solution in more detail than presented in [16] and [17], and explains the above-mentioned wheel acceleration constraint through discussions and simulations.

This brief is organized as follows. Section II formulates the PTC problem and presents a mathematical model of

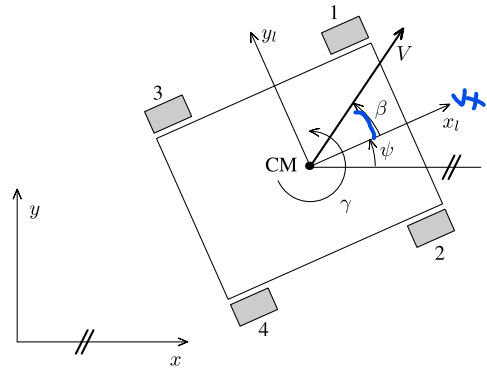


Fig. 1. Depiction of the kinematic quantities of the 4WS4WD EV.

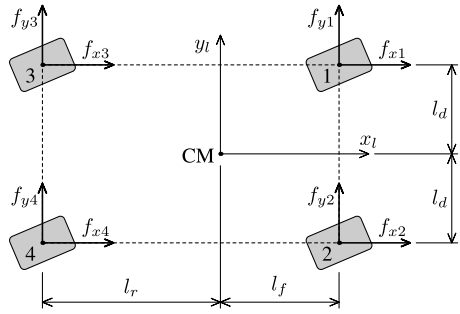


Fig. 2. Vehicle dimensions and tire-road friction forces.

the vehicle. Section III presents the PTC solution. Section IV presents the wheel acceleration constraint, and explains how to use this constraint. Section V presents simulation results from the application of the PTC and the constraint on an example 4WS4WD EV. Section VI concludes this brief by listing some possible future directions.

II. PROBLEM FORMULATION AND MATHEMATICAL MODEL

The following assumption is common to the existing works on the PTC of a 4WS4WD EV.

Assumption 1: The EV is a rigid body moving on a level surface; its pitch and roll degrees of freedom are neglected.

The PTC problem is that the coordinates $(x(t), y(t), \psi(t))$ of the center of mass (CM) of the EV in the Earth-fixed coordinate system need to track reference values $(x_{\text{ref}}(t), y_{\text{ref}}(t), \psi_{\text{ref}}(t))$ [11], [12] (Fig. 1).

Note that [8], [9], and [13] specify a piecewise circular path and need the EV to be oriented tangentially to this path. On the other hand, the path-tracking problem posed above is more general: specifying $(x_{\text{ref}}(t), y_{\text{ref}}(t))$ is equivalent to specifying a piecewise circular path, while specifying $\psi_{\text{ref}}(t)$ permits tangential as well as other orientations.

A mathematical model is a starting point for control system design problems. One important contribution of [8], [9], and [12] is a comprehensive mathematical model of the 4WS4WD EV. This brief uses, with slight modifications, the model compiled by [8] and [9]. The subscripts x_j and y_j , $j = 1, \dots, 4$, on a quantity mean that the quantity is expressed in the vehicle-fixed coordinate frame $x_l - y_l$.

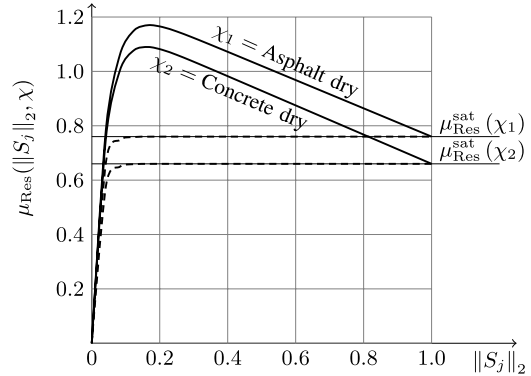


Fig. 3. Sample $\mu_{\text{Res}}(\|S_j\|_2, \chi)$ for a pneumatic tire on two road conditions χ [21, pp. 319–322], and the corresponding conservative approximations shown as dashed lines.

Following Assumption 1, the mathematical model of the 4WS4WD EV has essentially four components. These are vehicle body dynamics, wheel dynamics or driving motor dynamics, relation between slips and tire-road friction forces, and steering motor dynamics or kinematics. As in [8] and [12], aerodynamic drag is assumed to be absent.

The *vehicle body dynamics* is given by [20]

$$m(\dot{v}_{xl} - \gamma v_{yl}) = f_{x1} + f_{x2} + f_{x3} + f_{x4} \quad (1a)$$

$$m(\dot{v}_{yl} + \gamma v_{xl}) = f_{y1} + f_{y2} + f_{y3} + f_{y4} \quad (1b)$$

$$\begin{aligned} J_z \ddot{\psi} &= l_d(-f_{x1} + f_{x2} - f_{x3} + f_{x4}) \\ &+ l_f(f_{y1} + f_{y2}) - l_r(f_{y3} + f_{y4}) \end{aligned} \quad (1c)$$

where v_{xl} and v_{yl} are the projections of V on the x_l and y_l axes, respectively. That is, $v_{xl} = v \cos \beta$ and $v_{yl} = v \sin \beta$. Here, $v = \|V\|_2$, $\|\cdot\|_2$ represents the Euclidean norm, and V and β are as in Fig. 1. J_z is the moment of inertia of the vehicle about an axis through its CM, normal to the plane of the paper, and m is the mass of the vehicle. The vehicle's dimensions and the tire-road friction forces f_{xj} and f_{yj} , $j = 1, \dots, 4$, are shown in Fig. 2. Note that (1) lead to the form of the vehicle body dynamics shown in [8] and [9].

The *driving motor dynamics* is given by

$$J_{mj} \dot{\omega}_j = T_j - r_{ej}(f_{yj} \sin \delta_j + f_{xj} \cos \delta_j) \quad (2)$$

with J_{mj} the moment of inertia of the j th driving motor-wheel combination referred to the motor shaft, T_j the torque developed by this motor, δ_j the j th steering angle, r_{ej} the effective radius of the j th wheel, ω_j the angular velocity of the j th motor-wheel combination, and $j = 1, \dots, 4$.

The f_{xj} and f_{yj} that figure in (1) and (2) are related to the *combined wheel slip* S_j as [21, pp. 323–324]

$$\begin{bmatrix} f_{xj} \\ f_{yj} \end{bmatrix} = f_{sj} \underbrace{\begin{bmatrix} \cos \beta_j & -k_{sj} \sin \beta_j \\ \sin \beta_j & k_{sj} \cos \beta_j \end{bmatrix} \frac{\mu_{\text{Res}}(\|S_j\|_2, \chi)}{\|S_j\|_2}}_{[\mu_{xj} \quad \mu_{yj}]^\top} S_j. \quad (3)$$

The use of combined slips in the PTC of vehicles has its advantages, as explained in detail in [8] and [9].

In (3), $[\mu_{xj} \quad \mu_{yj}]^\top$ is a vector of tire-road adhesion coefficients, $\mu_{\text{Res}}(\|S_j\|_2, \chi)$ is a scalar saturation function, as shown in Fig. 3, $k_{sj} \in [0.9, 0.95]$ is an attenuation factor

used to account for the presence of tire tread profile, the superscript \top represents matrix transpose, and β_j and S_j are defined below. The normal reaction forces f_{zj} in (3) are calculated considering the static weight transfer f_{szj} , pitch weight transfer, and roll weight transfer on to the j th wheel, $j = 1, \dots, 4$. Though the pitch and roll degrees of freedom are ignored in the vehicle model through Assumption 1, their effect on f_{zj} is included [20]. These normal forces can be written as [9]

$$F_z = (I_4 + GN)^{-1} F_{zs} \quad (4)$$

with

$$N = \begin{bmatrix} \mu_{x1} & \mu_{x2} & \mu_{x3} & \mu_{x4} \\ \mu_{y1} & \mu_{y2} & \mu_{y3} & \mu_{y4} \end{bmatrix}$$

$$F_z = [f_{z1} \ f_{z2} \ f_{z3} \ f_{z4}]^T$$

$$F_{zs} = [f_{zs1} \ f_{zs2} \ f_{zs3} \ f_{zs4}]^T$$

$$G = \frac{h}{2l_d} \begin{bmatrix} \frac{l_d}{l_f + l_r} & \frac{l_d}{l_f + l_r} & \frac{-l_d}{l_f + l_r} & \frac{-l_d}{l_f + l_r} \\ \frac{k_{f\phi}}{k_{f\phi} + k_{r\phi}} & \frac{-k_{f\phi}}{k_{f\phi} + k_{r\phi}} & \frac{k_{r\phi}}{k_{f\phi} + k_{r\phi}} & \frac{-k_{r\phi}}{k_{f\phi} + k_{r\phi}} \end{bmatrix}^T$$

Here, I_4 is a 4×4 identity matrix, h is the height of the CM, g is the acceleration due to gravity, and $k_{f\phi}$ and $k_{r\phi}$ are, respectively, the front and the rear roll stiffness.

The S_j appearing in (3) is defined as [21, p. 315]

$$S_j = \begin{bmatrix} S_{Lj} \\ S_{Sj} \end{bmatrix} = \begin{bmatrix} \frac{r_{ej}\omega_j \cos \alpha_j - \|V_j\|_2}{\max(r_{ej}\omega_j \cos \alpha_j, \|V_j\|_2)} \\ \frac{r_{ej}\omega_j \sin \alpha_j}{\max(r_{ej}\omega_j \cos \alpha_j, \|V_j\|_2)} \end{bmatrix} \quad (5)$$

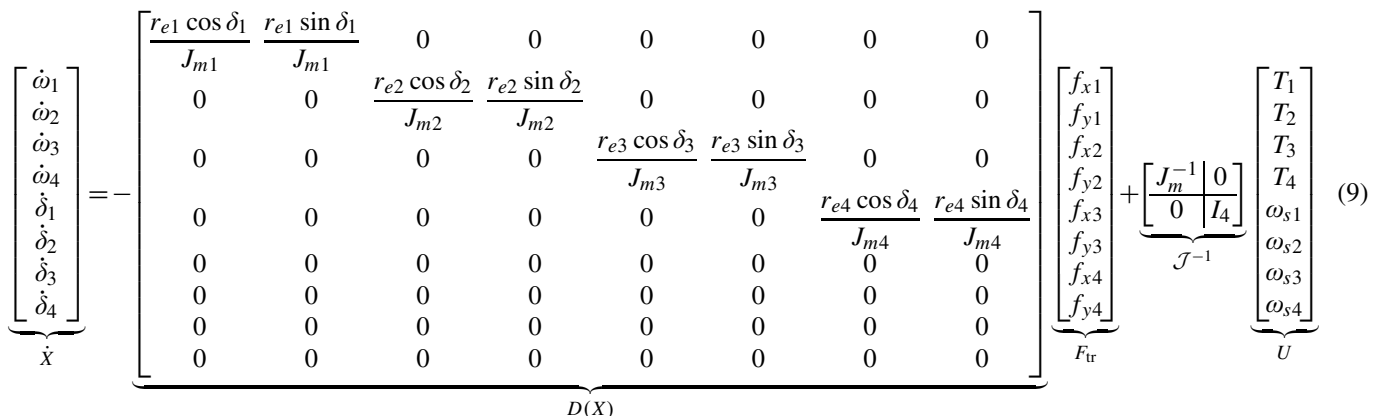
with

$$\alpha_j = \delta_j - \beta_j, \quad \beta_j = \angle(v_{xj} + iv_{yj}), \quad i = \sqrt{-1} \quad (6)$$

and

$$V_1 = \begin{bmatrix} v_{x1} \\ v_{y1} \end{bmatrix} = \begin{bmatrix} v_{xl} - l_d \gamma \\ v_{yl} + l_f \gamma \end{bmatrix}, \quad V_2 = \begin{bmatrix} v_{x2} \\ v_{y2} \end{bmatrix} = \begin{bmatrix} v_{xl} + l_d \gamma \\ v_{yl} + l_f \gamma \end{bmatrix} \quad (7a)$$

$$V_3 = \begin{bmatrix} v_{x3} \\ v_{y3} \end{bmatrix} = \begin{bmatrix} v_{xl} - l_d \gamma \\ v_{yl} - l_r \gamma \end{bmatrix}, \quad V_4 = \begin{bmatrix} v_{x4} \\ v_{y4} \end{bmatrix} = \begin{bmatrix} v_{xl} + l_d \gamma \\ v_{yl} - l_r \gamma \end{bmatrix}. \quad (7b)$$



dijadikan persamaan masing2 roda supaya lebih ringkas.

Persamaan (9) bukan model $Ax+Bu$, apakah bisa menggunakan MPC kontroler. Jika bisa, f nya gimana ?

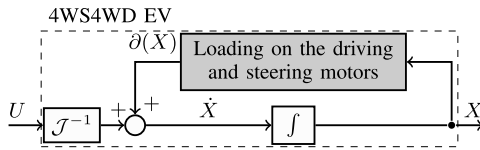


Fig. 6. Block diagram of Fig. 5 redrawn for the development of a DOB-based disturbance rejection scheme. $\partial(X)$ is the load on the driving and steering motors.

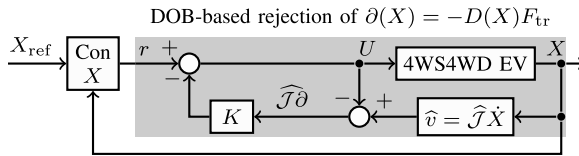


Fig. 7. Controller of X . This scheme drives the wheels of the vehicle at the desired angular speeds $\omega_{j\text{ref}}$ and desired steering angles $\delta_{j\text{ref}}$. $\text{Con } X$ stands for controller X . K is a diagonal matrix; it is an identity matrix for ideal disturbance rejection. The block named 4WS4WD EV is as in Fig. 6.

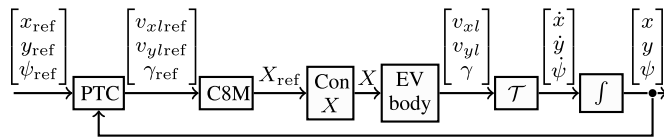


Fig. 8. Proposed PTC scheme for a 4WS4WD EV. C8M is the coordinator of the eight motors, $\text{Con } X$ is the controller of X , and T is a transformation matrix. T and f arise naturally when sensing (x, y, ψ) , and are not designed as part of the control scheme.

Fig. 5 presents a block diagrammatic representation of (1), (3)–(7), and (9). This block diagram reveals two natural feedback loops in the vehicle dynamics. Each loop provides its share of insights, as described in Sections III and IV. Note that while the mathematical model looks complicated and seems to justify treating it as $\dot{x} = f(x, u)$, $y = h(x, u)$, as done in [8], [9], [13], and [15], its block diagrammatic representation suggests that it may be amenable to a simpler treatment.

III. INSIGHTS FROM LOOP 1: PATH-TRACKING CONTROL

The block diagram of Fig. 5 can be redrawn in the form shown in Fig. 6 to reveal that the vehicle body dynamics essentially imposes a load $\partial(X)$ on the driving and steering wheels. This observation suggests that if $\partial(X)$ can be estimated and compensated using, e.g., a disturbance observer (DOB), then it becomes easier to control X to its reference value X_{ref} . That is, if the load imposed by the vehicle body on the driving and steering motors can be overcome, then these motors will track their desired ω_j and δ_j nicely. The block diagram of Fig. 7 shows a conceptual implementation of this idea of estimation, compensation, and control. This idea is explained in detail in Section III-A. Fig. 8 shows a PTC scheme that follows immediately from the above observation. It has three components that are described next.

A. Controller of X

This component is made of two loops, as shown in Fig. 7. The outer loop helps X track X_{ref} using a controller, denoted

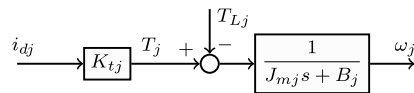


Fig. 9. Representation of a motor with the current i_j well controlled at the desired value i_{dj} . For permanent magnet dc motors, i_j is the armature current. For brushless dc motors i_j is the average dc bus current [22, p. 769]. B_j is the coefficient of viscous friction of the motor.

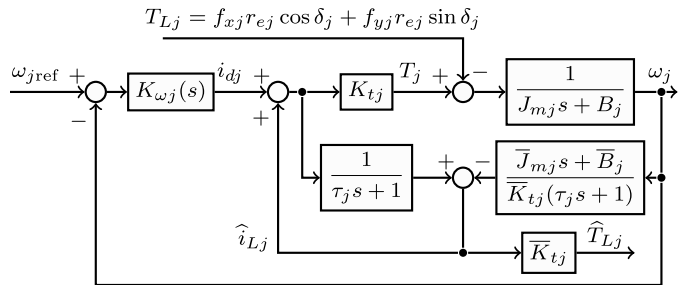


Fig. 10. DOB-based speed control system for the j th driving motor [23]. $K_{\omega j}(s)$ is the speed controller and K_{tj} is the torque constant of the motor. The pristine values of K_{tj} , J_{mj} , and B_j used in the DOB are, respectively, \bar{K}_{tj} , \bar{J}_{mj} , and \bar{B}_j . The estimate of T_{Lj} is \hat{T}_{Lj} .

$\text{Con } X$ in Fig. 7. The inner loop, which is the DOB-based disturbance rejection loop, is explained below, followed by details of its practical implementation.

From Fig. 6, the combination of wheel dynamics and vehicle body dynamics of the 4WS4WD EV is of the form $\dot{X} = \mathcal{J}^{-1}U + \partial(X) = \mathcal{J}^{-1}(U + \mathcal{J}\partial(X))$, with $\partial(X) = -D(X)F_{\text{tr}}(X)$, and $\mathcal{J} = (\mathcal{J}^{-1})^{-1}$. From Fig. 7, assuming very little uncertainty in the estimate $\widehat{\mathcal{J}}$ of \mathcal{J} , i.e., assuming $\widehat{\mathcal{J}} = \mathcal{J}$, and using the fact that K and \mathcal{J} are diagonal and invertible, the equation of the 4WS4WD EV with the DOB-based disturbance rejection scheme is

$$\dot{X} = (I - K)\partial(X) + \mathcal{J}^{-1}r. \quad (10)$$

Equation (10) shows that the closer K is to I , the better is $\partial(X)$ rejected. As (9) is in decoupled form, the DOB-based speed control structure can be implemented separately for each driving motor, instead of as in Fig. 7. The steering motors do not need DOB, as the equations corresponding to the steering motors in (10) are the same as in (8).

Described here is the DOB-based control of X that is proposed to be actually used in practice on the driving and steering motors of the 4WS4WD EV. Fig. 9 shows the simplified block diagram of a permanent magnet motor assuming the motor current to be well regulated. The driving motor speed controller of Fig. 10 has two parts: 1) a PID controller $K_{\omega j}(s)$ for quality of response and 2) a DOB for disturbance rejection. In the simulations, MATLAB/Simulink's PID tuner is used in the first step to obtain an acceptable response from the control system of Fig. 10 in the absence of T_{Lj} and \hat{i}_{Lj} . Then, in the second step, T_{Lj} and \hat{i}_{Lj} are connected. The $1/\tau_j$ in the DOB is at least such that ω_j tracks $\omega_{j\text{ref}}$ with the DOB and the load T_{Lj} present, approximately as well as it tracks $\omega_{j\text{ref}}$ with them absent; $1/\tau_j$ is at most such that it can filter out measurement noise. Under Assumption 2, each steering motor is a single integrator plant; therefore, any first-order controller with a high dc gain gives good position control. Thus, the

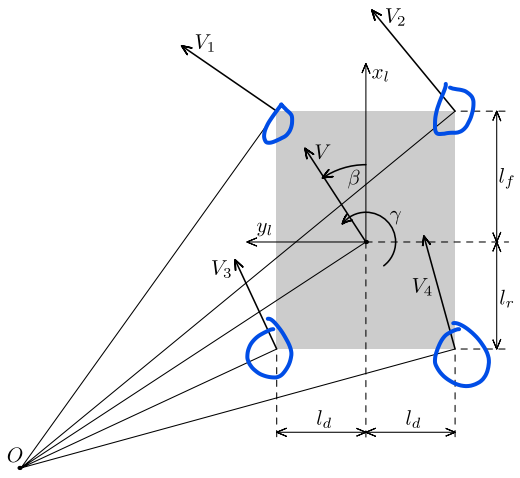
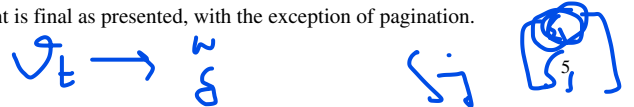


Fig. 11. Velocities of various points of the EV, which is assumed as a rigid body moving with yaw rate γ and velocity vector V of the CM. The normals to the velocity vectors of points on the body intersect at a common point O known as ICM.

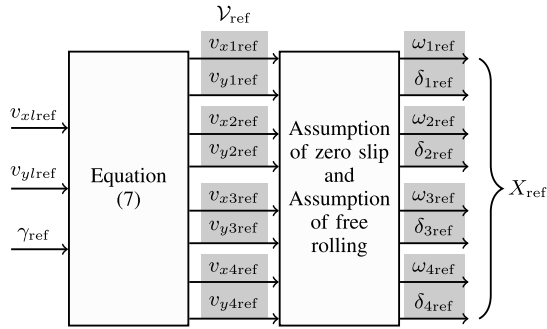


Fig. 12. Coordinator of the eight motors.

discussion of the design of controller for the steering motor is omitted.

B. Coordinator of the Eight Motors

This component is implemented as an open loop. It assigns the reference values $\omega_{j\text{ref}}$ and $\delta_{j\text{ref}}$, which are the elements of X_{ref} , to the driving and steering MCSs with the goal that the CM of the EV track the desired values $v_{x\text{lref}}(t)$, $v_{y\text{lref}}(t)$, and $\gamma_{\text{ref}}(t)$ of v_{xl} , v_{yl} , and γ .

The DOB-based speed control structure discussed in Section III-A helps the motors achieve any speeds, which are permitted by the ratings of the motors and the amplifiers, assuming that the vehicular load is within the capabilities of the motors. However, only if the motors are driven and steered at the appropriate speeds $\omega_{j\text{ref}}$ and angles $\delta_{j\text{ref}}$ does the vehicle move with the desired v_{xl} , v_{yl} , and γ . In this brief, the wheels are driven and steered using the concept of instantaneous center of motion (ICM).

It can be shown that under Assumption 1 the j th corner of the EV has velocity vector V_j , as shown in Fig. 11 and given by (7). In this brief, the j th wheel is driven and steered such that the desired velocity of its center equals V_j , with V_j as in Fig. 11. For this purpose, the appropriate $\omega_{j\text{ref}}$ and $\delta_{j\text{ref}}$ are calculated using the following assumptions [11], [12].

Assumption 3 (Zero Slip): The wheel plane coincides with V_j , i.e., $\alpha_j = 0$, implying $\delta_{j\text{ref}} = \angle(v_{xj\text{ref}} + iv_{yj\text{ref}})$.

Assumption 4 (Free Rolling): Longitudinal slip S_{lj} equals zero, implying $\omega_{j\text{ref}} = (v_{xj\text{ref}}^2 + v_{yj\text{ref}}^2)^{1/2}/r_{ej}$.

Section III-D discusses the validity of these assumptions. The ICM approach is used by the coordinator of the eight motors shown in Fig. 12.

C. Path-Tracking Controller

This component is implemented using feedback. It helps (x, y, ψ) track $(x_{\text{ref}}, y_{\text{ref}}, \psi_{\text{ref}})$. Fig. 1 shows that

$$-T \begin{bmatrix} \dot{x} \\ \dot{y} \\ \dot{\psi} \end{bmatrix} = T \begin{bmatrix} v_{xl} \\ v_{yl} \\ \gamma \end{bmatrix}, \quad T = \begin{bmatrix} \cos \psi & -\sin \psi & 0 \\ \sin \psi & \cos \psi & 0 \\ 0 & 0 & 1 \end{bmatrix}. \quad (11)$$

Under Assumptions 3 and 4, and assuming a well-controlled X , the nominal gain from $[v_{x\text{lref}} \ v_{y\text{lref}} \ \gamma_{\text{ref}}]^T$ to $[v_{xl} \ v_{yl} \ \gamma]^T$ is simply an identity matrix; therefore, the path-tracking controller needs only to be designed for (11). The specific design used in this brief is presented in Fig. 13.

Fig. 13 shows why this PTC system promises to be relatively simple to tune in practice too, at least at small slips (up to about 2%–3%). The j th MCS, which comprises a driving and a steering MCS, can be tuned independently of the PTC system. Thus, effectively, there are only the three controllers $C_x(s)$, $C_y(s)$, and $C_\psi(s)$ to tune. In this brief, these controllers are PID. For small slips, and assuming a good sensing of ψ , which would give a good T^{-1} , the gain from the output of these controllers to the vector $[\dot{x} \ \dot{y} \ \dot{\psi}]^T$ can be approximately unity. Considering this gain as the nominal gain, the closed-loop system is nominally a collection of three single-integrator plant control systems, and is therefore nominally stable. In addition, these nominal conditions allow the three controllers to have the same structure and parameter values, as shown in Table I, further simplifying the tuning of these controllers.

In Fig. 13, the signals that need to be measured are x , y , and ψ , which can be measured as in [12], and ω_j and δ_j , $j = 1, \dots, 4$.

D. Remarks on the ICM Approach and Assumptions 3 and 4

In reality, the vehicle moves, and thus the vector $[v_{xl} \ v_{yl} \ \gamma]^T$ arises only if slips exist, as shown in Fig. 5, and not through zero slip and free rolling. However, free rolling condition and absence of slips seem to be common assumptions in the vehicle control literature at the controller design stage, and seem to give acceptable results. Ploeg *et al.* [11] too have made these assumptions, while Ploeg *et al.* [12] have accounted for the slips at this stage. Interestingly, the results in [12] are not superior to those in [11]; the position and yaw angle errors of the vehicle are larger in [12] than in [11]. Ackermann [24, p. 174] too ignores slips with the justification that the longitudinal slip is smaller than 2% under normal driving conditions. In this context, it would be interesting to see the slips up to which the PTC scheme works.

In the ICM way of coordinating the four wheels $\delta_{j\text{ref}}$ is undefined when $v_{xj\text{ref}} = v_{yj\text{ref}} = 0$. This situation corresponds

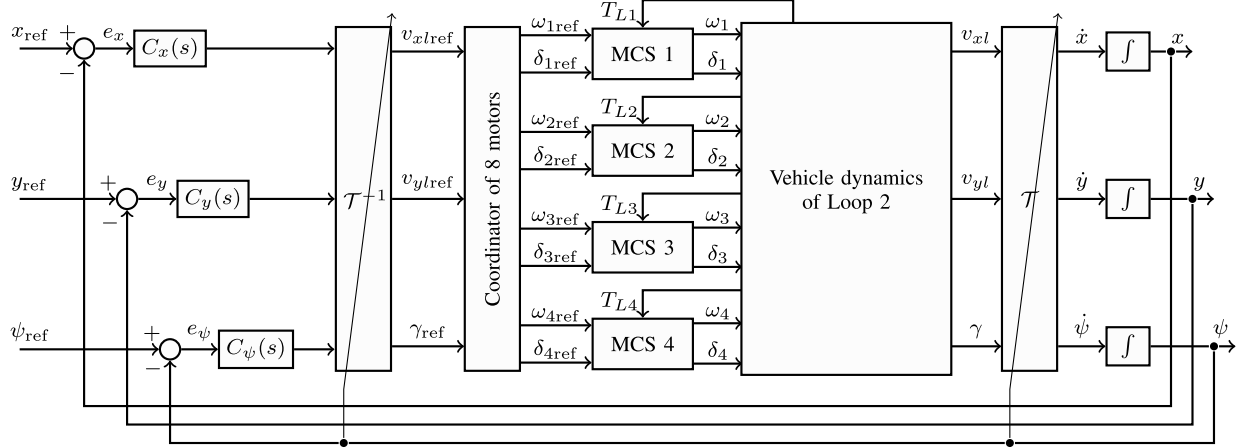


Fig. 13. Simulation diagram showing an implementation of the PTC system of Fig. 8. $C_x(s)$, $C_y(s)$, and $C_\psi(s)$ are PID. MCS 1, ..., MCS 4 are as explained in the second half of Section III-A. The \mathcal{T} and \mathcal{T}^{-1} blocks are updated using ψ . The block named *Vehicle dynamics of Loop 2* comprises Loop 2 shown in Fig. 5.

to the ICM occurring at the center of the j th wheel. One way to get around this situation is to admit only those reference trajectories that do not cause the ICM coordinates $(-v_{yl\text{ref}}/\gamma\text{ref}, -v_{xl\text{ref}}/\gamma\text{ref})$ in the vehicle-fixed coordinate frame to equal any one of (l_f, l_d) , $(l_f, -l_d)$, $(-l_r, l_d)$, and $(-l_r, -l_d)$, which are the coordinates in the vehicle-fixed coordinate frame of the first, second, third, and fourth wheel centers, respectively. Another way to get around this situation is to have $v_{xj\text{ref}}$ and $v_{yj\text{ref}}$ keep their previous values when both of them equal zero. Alternatively, Ploeg *et al.* [12] get around this situation by requiring that $(v_{xj\text{ref}}^2 + v_{yj\text{ref}}^2)^{1/2} > 0$. There are yet other solutions [25]. Thus, under the ICM approach, the maneuverability of the EV is reduced somewhat, where a different approach might have allowed the EV to be fully maneuverable. However, the simplicity of this approach and its good performance demonstrated in [12] make it attractive.

E. Comparison

Ploeg *et al.* [26] outline a path-tracking control scheme that resembles the scheme shown in this brief. However, [26] does not present the mathematical model of the vehicle and the details of how the motors are coordinated. The ideas of [26] seem to have been developed and extended in [27]. Presented here is a comparison with [27].

There are two similarities between this brief and [27].

- 1) Both works see the vehicle body dynamics as loading the individual motors, and their control algorithms reject this load to coordinate the eight motors.
- 2) Both works consider the ICM approach to coordinate the eight motors.

However, [27] does not use the ICM approach in the eventual PTC, choosing instead explore a method that might allow greater maneuverability of the EV. The remainder of this section shows that this brief differs from [27] in additional important ways.

Leenen [27] uses a so-called *dynamic inverse algorithm* (DIA) as the coordinator of the eight motors. The DIA minimizes a quadratic objective function over the space of

$\omega_{j\text{ref}}$ and $\delta_{j\text{ref}}$ to generate $\omega_{j\text{ref}}$ and $\delta_{j\text{ref}}$. The DIA involves more than 2300 floating point operations (flops) in each sampling interval, while the ICM way of coordinating the eight motors involves about 60 flops in each sampling interval.

Each of the individual controllers in the path-tracking controller in this brief acts on a plant that is nominally a single integrator, as shown in Section III-C. On the other hand, the path-tracking controller of [27] acts on a plant that is a 3×3 matrix, labeled slave control level in [27, p. 48], in which each input affects all the outputs in a complicated manner. Therefore, in practice, the controller developed in this brief may be easier to tune than that developed in [27].

The stability of the closed-loop PTC system with the DIA is unclear as admitted in [27, p. 47]. On the other hand, the control system proposed in this brief is at least nominally stable, as shown in Section III-C.

IV. INSIGHTS FROM LOOP 2: WHEEL SLIP CONSTRAINTS

The PTC scheme developed in the previous section assumes zero slips, and might suggest that X can take arbitrary values. In reality, wheel acceleration exceeding a certain value could result, e.g., in the vehicle moving very little from standstill. Thus, magnitude of \dot{X} needs to be constrained. What is the maximum value of $\|S_j\|_2$ for a given magnitude of \dot{X} ? This question is answered here using Loop 2 of Fig. 5.

A. Decomposition into Wheel Subsystems

DOB-based disturbance rejection can easily be tuned for X to track X_{ref} well in the face of disturbances, giving $X \approx X_{\text{ref}}$. Further, under Assumptions 3 and 4, X_{ref} is equivalent to the vector \mathcal{V}_{ref} in terms of information content. Therefore, $\mathcal{V}_{\text{ref}} \approx X_{\text{ref}} \approx X$. Thus, \mathcal{V}_{ref} needs to be constrained to constrain X .

In Loop 2 of Fig. 5, the slip vector S_j is essentially a vector of normalized errors. This loop can be viewed as a feedback control system in which the plant output \mathcal{V} needs to track the reference input \mathcal{V}_{ref} . The theory of input-to-state stability (ISS) [28] can help develop bounds on \mathcal{V}_{ref} such that $\mathcal{V}_{\text{ref}} - \mathcal{V}$, and, consequently, $\|S_j\|_2$ are bounded.

An examination of the ISS of the full vehicle is very tedious. The 4WS4WD EV can instead be viewed as a collection of four wheel subsystems, and the j th subsystem can be analyzed for stability. Decomposing a vehicle analysis and design problem into that of analysis and design of wheel subsystems has been done in [29] for active suspension systems, and in [11] and [12] for 4WS4WD EVs. As in [12], the wheel-ground contact forces f_{xj} and f_{yj} can be viewed as accelerating an equivalent mass m_j , which is related to the normal load f_{zj} as $m_j = f_{zj}/g$, $g = 9.8 \text{ m/s}^2$, according to

$$m_j \dot{v}_{xj} = f_{xj}, \quad m_j \dot{v}_{yj} = f_{yj}. \quad (12)$$

This decomposition is used next. Note that for the purpose of the following development, m_j does not need to be expressed in terms of the weight transfer, as done in [11] and [12].

B. Maximum Value of $\|S_j\|_2$ for Given Value of $\|\dot{V}_{j\text{ref}}\|_2$

What is the maximum value of $\|S_j\|_2$ for a given value of $\|\dot{V}_{j\text{ref}}\|_2$, $V_{j\text{ref}} = [v_{xj\text{ref}} \ v_{yj\text{ref}}]^T$? This question is answered here for a wheel subsystem. This answer, in turn, helps select the limits on $\ddot{x}_{\text{ref}}(t)$, $\ddot{y}_{\text{ref}}(t)$, and $\ddot{\psi}_{\text{ref}}(t)$.

Through a series of manipulations using (6) and the approximation $\mathcal{V}_{\text{ref}} \approx X_{\text{ref}} \approx X$, (3) and (12) give, for $k_{sj} = 1$

$$\begin{bmatrix} \dot{E}_{xj} \\ \dot{E}_{yj} \end{bmatrix} = -\mu_{\text{Res}}(\|S_j\|_2, \chi) g \begin{bmatrix} \frac{E_{xj}}{\sqrt{E_{xj}^2 + E_{yj}^2}} \\ \frac{E_{yj}}{\sqrt{E_{xj}^2 + E_{yj}^2}} \end{bmatrix} + \begin{bmatrix} \dot{v}_{xj\text{ref}} \\ \dot{v}_{yj\text{ref}} \end{bmatrix} \quad (13)$$

where

$$E_j = \begin{bmatrix} E_{xj} \\ E_{yj} \end{bmatrix} \triangleq \begin{bmatrix} v_{xj\text{ref}} - v_{xj} \\ v_{yj\text{ref}} - v_{yj} \end{bmatrix}.$$

Consider the dashed curves shown in Fig. 3. These curves are described by

$$\mu(\|S_j\|_2, \chi) = \mu_{\text{Res}}^{\text{sat}}(\chi) [1 - e^{-c\|S_j\|_2}] \quad (14)$$

with

$$\mu_{\text{Res}}^{\text{sat}}(\chi) = \mu_{\text{Res}}(\|S_j\|_2 = 1, \chi), \quad c > 0.$$

The following constraint, derived using the theory of ISS applied to (13), answers the above question:

$$\|S_j\|_2 \leq \frac{\sqrt{2}}{c} \ln \left(\frac{1}{1 - \frac{1}{\theta g \mu_{\text{Res}}^{\text{sat}}} \sup_{t_0 \leq \tau \leq t} \|\dot{V}_{j\text{ref}}(\tau)\|_2} \right) \quad (15)$$

with $0 < \theta < 1$. The derivation is omitted for want of space. In Fig. 14, the solid curve represents (15) with $\theta = 0.99999$, $c = 50$, and $\mu_{\text{Res}}^{\text{sat}} = 0.74$. It can be verified that the curves for smaller values of θ lie above this curve. Thus, the least upper bound on $\|S_j\|_2$ using (15) is achieved for $\theta = 1$.

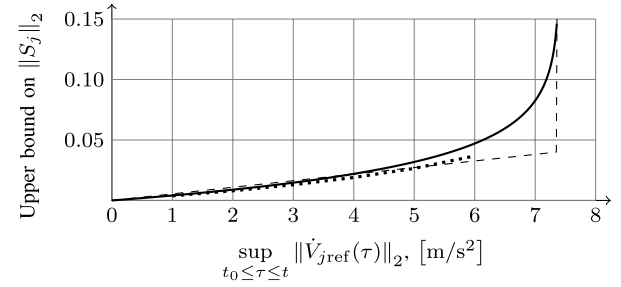


Fig. 14. Constraints on $\|S_j\|_2$. The solid curve represents (15). It says that when a wheel with a pneumatic tire travels on dry asphalt, limiting the wheel's acceleration to, e.g., 6 m/s^2 suffices for $\|S_j\|_2 \leq 5\%$. Section IV-C discusses the dashed curve. Section V-B discusses the dotted curve.

C. How to Use the Constraint

The constraint of (15) can be used to find maximum permissible acceleration $\|\dot{V}_{j\text{ref}}\|_2$ through the following procedure.

- 1) For the surface on which the EV needs to travel, identify a $\mu_{\text{Res}} - \|S_j\|_2$ curve such as those in Fig. 3.
- 2) Identify $\mu_{\text{Res}}^{\text{sat}}$ and a suitable c for this curve as in (14).
- 3) Plot \mathcal{S} versus \mathcal{A} using $\mathcal{S} = -(\sqrt{2}/c) \ln(1 - \mathcal{A}/\mu_{\text{Res}}^{\text{sat}} g)$.
- 4) The value of \mathcal{A} corresponding to a desired maximum value \mathcal{S} of $\|S_j\|_2$ is the maximum permissible acceleration $\|\dot{V}_{j\text{ref}}\|_2$.

A simplification can be achieved in this procedure by observing as follows. Imagine that the μ_{Res} axis of Fig. 3 is multiplied by g , and that then the $\|S_j\|_2$ and $\mu_{\text{Res}} g$ axes are exchanged. Then, the dashed curve on these new axes corresponding to $\mu_{\text{Res}}^{\text{sat}} = 0.74$ would roughly correspond to the solid curve of Fig. 14. A sharper knee on this dashed curve would have allowed it to capture the information in the $\mu_{\text{Res}}(\cdot)g$ versus $\|S_j\|_2$ curves more accurately in the region $\|S_j\|_2 \leq 0.04$. Ideally, this dashed curve would be such that it would result in the piece-wise linear dashed curve of Fig. 14.

The above observation suggests the following simplified procedure.

- 1) For the surface on which the EV needs to travel, identify a $\mu_{\text{Res}} - \|S_j\|_2$ curve such as those in Fig. 3.
- 2) Identify $\mu_{\text{Res}}^{\text{sat}}$.
- 3) Multiply the μ_{Res} axis by g .
- 4) Determine slip \mathcal{S}_0 corresponding to $\mu_{\text{Res}}^{\text{sat}} g$ in the low-slip region.
- 5) For any slip \mathcal{S}_1 between 0 and \mathcal{S}_0 , identify the corresponding value of $\mu_{\text{Res}} g$; this value is the maximum permissible acceleration $\|\dot{V}_{j\text{ref}}\|_2$ for this \mathcal{S}_1 .

This procedure allows identifying the permissible $\|\dot{V}_{j\text{ref}}\|_2$ for a given $\|S_j\|_2$ immediately from Fig. 3, and helps avoid constructing the solid curve of Fig. 14.

V. SIMULATION RESULTS

The simulation diagram of Fig. 13 is used along with the data of Table I. The Burckhardt model for dry asphalt $\mu_{\text{Res}} = 0.857(1 - e^{-33.822\|S_j\|_2}) - 0.347\|S_j\|_2$ [21, pp. 319–322] is used. Two kinds of simulations are performed: 1) tracking a figure 8 to observe the behavior of the motor speeds, steering angles, tracking errors, and slips, and

TABLE I
VALUES OF THE PARAMETERS USED IN THE SIMULATIONS

Parameter	Value
$k_{r\phi}$	20972 $\frac{\text{N}\cdot\text{m}}{\text{rad}}$ [9]
$k_{f\phi}$	50539 $\frac{\text{N}\cdot\text{m}}{\text{rad}}$ [9]
$L_d = t_1, t_2$	0.75 m
$l_r = l_f$	1.42 m
h	0.42 m
m	1000 kg
$K_{tj} = \bar{K}_{tj}$	2 N·m/A
$J_{mj} = \bar{J}_{mj}$	0.36 kg·m ² [27]
τ_j	0.001 s
$C_x(s), C_y(s), C_\psi(s)$	$\frac{100s+1}{10s+1}$
$K_{\omega j}(s)$	$30 + \frac{60}{s}$
g	9.8 m/s ²
Sampling period	0.0001 s

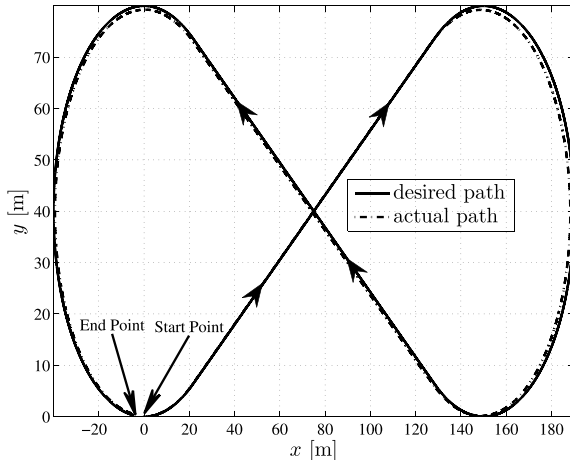


Fig. 15. Figure 8 to be tracked and the actual path taken.

2) tracking a circle to verify the constraint of Section IV-B.
The following sections present the results.

A. Tracking a Figure 8

The EV needs to track a figure 8 that is shown in Fig. 15 with tangential speed given by the expression $v_t(t) = 16(1 - 0.9e^{-0.3t})$. The EV has an initial speed of 1.6 m/s. As the circular parts of the figure have a radius of $r_t = 40$ m, the EV has a centripetal acceleration of $v_t^2/r_t = 6.4$ m/s² on these sections. The total acceleration $((v_t^2/r_t)^2 + (dv_t/dt)^2)^{1/2}$ of the EV does not exceed 6.4 m/s²; so from the dashed curve of Fig. 14, or from Fig. 3 using the second procedure described in Section IV-C, it follows that $\|S_j\|_2 < 0.04$.

Fig. 16 shows that the tracking errors are $|e_x| < 3$ m, $|e_y| < 1.5$ m, and $|e_\psi| < 4^\circ$. When tracking the figure 8 with smaller steady-state accelerations, these errors are proportionately smaller. In the simulations, proportional integral controllers did not result in stable PTC at this acceleration. Therefore, proportional derivative controllers are used, because they are known for damping. This behavior also shows that the plant that $C_x(s)$ or $C_y(s)$ or $C_\psi(s)$ sees is only nominally a single integrator, and that there is slips-related uncertainty in the plant model, which needs to be quantified. Full PID control for the PTC may help reduce the tracking error, and is under investigation.

Note that each time the CM of the EV crosses from a circular section to a straight line section of the path, or from a

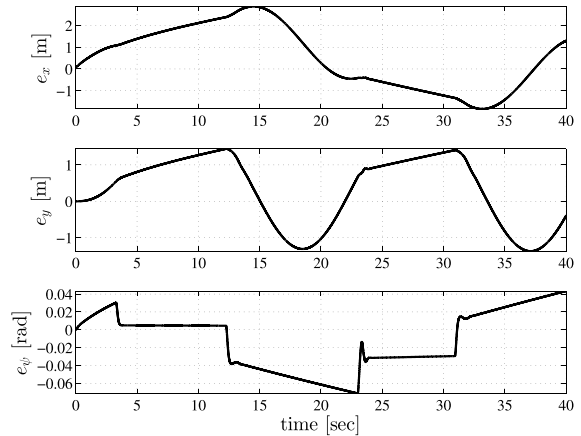


Fig. 16. Tracking errors.

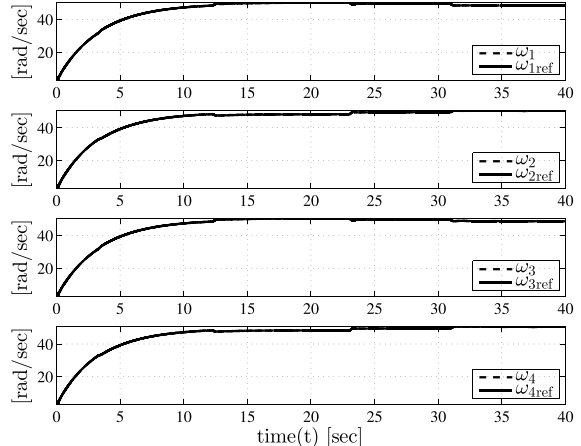


Fig. 17. Driving wheel speeds.

straight line section to a circular section, the EV's acceleration changes almost abruptly as the centripetal component appears or disappears. There are five sections and four crossings. The effect of these changes is prominent in the steering angles of Fig. 18 and the slips of Fig. 19, and not in the wheel speeds of Fig. 17. This behavior needs further examination. Except for these transients at the crossings, during the steady-state phase on a section, the behavior of ω_j , δ_j , and $\|S_j\|_2$ is as expected. Specifically, the slips are at most around 0.04 on the circular parts, and near zero on the straight line parts; the outer wheels have higher speeds and lower steering angles on the circular parts, and all wheels have the same speeds and steering angles on the straight line parts.

In Fig. 19, the slips at the start of the simulation are nearly 20% and seem to contradict the constraint of (15). However, note that the constraint of (15) is applicable only during quasi-static conditions, because the values of μ_{Res} in Fig. 3 are valid only for quasi-static operating points, and not for quickly changing dynamic transition states [21, p. 321]. For example, if the vehicle starts from standstill, $S_{Lj} = 1$ from (5). The constraint of (15) is not applicable here.

B. Tracking a Circle

The question that is needed to be answered through this simulation is whether the maximum value of $\|S_j\|_2$ at each

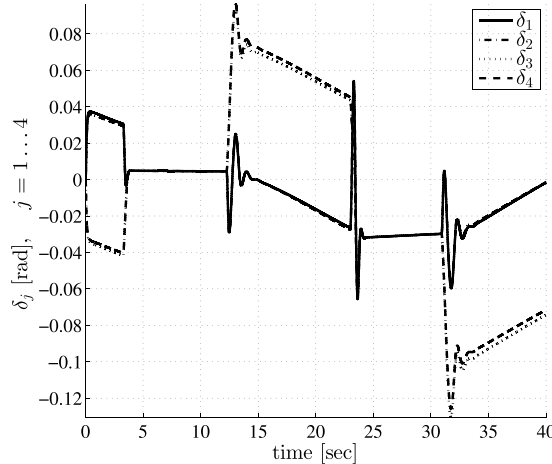


Fig. 18. Steering angles.

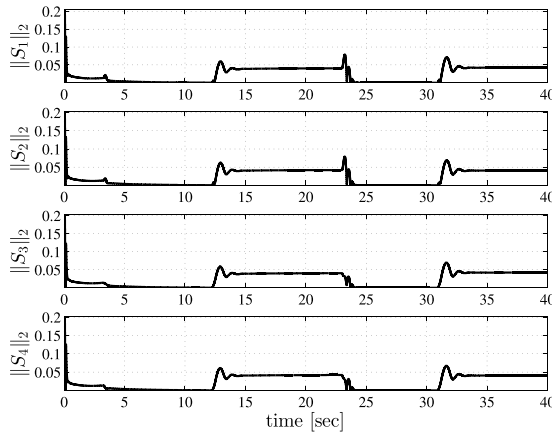


Fig. 19. Magnitudes of the combined wheel slips.

value of centripetal acceleration is as predicted by the solid or dashed curves of Fig. 14. The results of this simulation are plotted as a dotted curve in Fig. 14. This curve is closer to the dashed curve, and suggests that the solid curve is conservative near its knee. The control system works stably for centripetal accelerations up to about 6.4 m/s^2 . A problem for future investigation is how to stabilize the PTC at $\|S_j\|_2 > 6.4 \text{ m/s}^2$.

Overall, the simulation results are encouraging, and suggest that the PTC system may perform well in practice too.

VI. CONCLUSION

This brief has performed a block-diagrammatic examination of the mathematical model of a 4WS4WD EV to reveal the underlying physical interactions. This revelation enabled the development of a conceptually simple PTC scheme for an autonomous version of this EV. This simplicity is expected to help implement the controller relatively easily on the real EV. In contrast, previous works did not notice any structure in the mathematical model of this EV beyond the form $\dot{x} = f(x, u)$, $y = h(x, u)$, and thus used mathematically sophisticated controllers for path-tracking. However, mathematically sophisticated controllers can be difficult to tune in practice.

The path-tracking strategy shown here comprises essentially two steps. First, the driving and steering motors are controlled

for good performance and disturbance rejection. Next, these MCSs are wrapped in an outer loop that coordinates them for path-tracking with \ddot{x}_{ref} , \ddot{y}_{ref} , and $\ddot{\psi}_{\text{ref}}$ restricted by the user, which restricts the wheel accelerations, which in turn restricts wheel slips. To use this control strategy, the surface would need to be homogeneous and known *a priori*. Future work can investigate how to vary the constraint on wheel accelerations online with variations in the surface.

The PTC scheme developed here assuming zero slips and free rolling works well in simulation for $\|S_j\|_2 \leq 6.4\%$ on dry asphalt. These slips introduce uncertainty into the nominal unity-gain model that is assumed between $[v_{x\text{ref}} \ v_{y\text{ref}} \ \psi_{\text{ref}}]^T$ and $[v_{x\text{l}} \ v_{y\text{l}} \ \gamma]^T$ in Section III-C. The connection between wheel slips and model uncertainty needs to be investigated.

In this PTC system, only the driving motors are used to compensate for the load offered by the vehicle. It is desirable to use both the driving and steering motors to compensate for the load on each wheel unit [24, pp. 171–176].

ACKNOWLEDGMENT

The authors would like to thank Dr. P. Wahi, IIT Kanpur, and the editors and anonymous reviewers for helping improve this brief.

REFERENCES

- [1] H. Peng and H. Jwu-Sheng, “Traction/braking force distribution for optimal longitudinal motion during curve following,” *Vehicle Syst. Dyn., Int. J. Vehicle Mech. Mobility*, vol. 26, no. 4, pp. 301–320, 1996.
- [2] Y. Furukawa, N. Yuhara, S. Sano, H. Takeda, and Y. Matsushita, “A review of four-wheel steering studies from the viewpoint of vehicle dynamics and control,” *Vehicle Syst. Dyn., Int. J. Vehicle Mech. Mobility*, vol. 18, nos. 1–3, pp. 151–186, 1989.
- [3] Nissan Pivo. (2013). [Online]. Available: http://en.wikipedia.org/wiki/Nissan_Pivo
- [4] Eze Corporation SmartWheel. (2013). [Online]. Available: <http://www.youtube.com/user/EzeSmartWheel>
- [5] Siemens VDO eCorner Project. (2013). [Online]. Available: <http://www.youtube.com/watch?v=8tLQ2-yKT4Y>
- [6] M. Jonasson and J. Andreasson, “Exploiting autonomous corner modules to resolve force constraints in the tyre contact patch,” *Vehicle Syst. Dyn., Int. J. Vehicle Mech. Mobility*, vol. 46, no. 7, pp. 553–573, Jul. 2008.
- [7] R. Grepil, J. Vejlupek, V. Lambersky, M. Jasansky, F. Vadlejch, and P. Coupek, “Development of 4WS/4WD experimental vehicle: Platform for research and education in mechatronics,” in *Proc. IEEE Int. Conf. Mechatron.*, Istanbul, Turkey, Apr. 2011, pp. 893–898.
- [8] S.-T. Peng, “On one approach to constraining the combined wheel slip in the autonomous control of a 4WS4WD vehicle,” *IEEE Trans. Control Syst. Technol.*, vol. 15, no. 1, pp. 168–175, Jan. 2007.
- [9] S.-T. Peng, C.-C. Chang, and J.-J. Sheu, “On robust bounded control of the combined wheel slip with integral compensation for an autonomous 4WS4WD vehicle,” *Vehicle Syst. Dyn., Int. J. Vehicle Mech. Mobility*, vol. 45, no. 5, pp. 477–503, May 2007.
- [10] C. Liu, M. Wang, and J. Zhou, “Coordinating control for an agricultural vehicle with individual wheel speeds and steering angles [Applications of Control],” *IEEE Control Syst. Mag.*, vol. 28, no. 5, pp. 21–24, Oct. 2008.
- [11] J. Ploeg, J. P. M. Vissers, and H. Nijmeijer, “Control design for an overactuated wheeled mobile robot,” in *Proc. 4th IFAC Symp. Mechatron. Syst.*, Heidelberg, Germany, Sep. 2006, pp. 127–132.
- [12] J. Ploeg, H. E. Schouten, and H. Nijmeijer, “Position control of a wheeled mobile robot including tire behavior,” *IEEE Trans. Intell. Transp. Syst.*, vol. 10, no. 3, pp. 523–533, Sep. 2009.
- [13] H. Yang, V. Cocquempot, and B. Jiang, “Optimal fault-tolerant path-tracking control for 4WS4WD electric vehicles,” *IEEE Trans. Intell. Transp. Syst.*, vol. 11, no. 1, pp. 237–243, Mar. 2010.
- [14] D.-Y. Li, Y.-D. Song, D. Huang, and H.-N. Chen, “Model-independent adaptive fault-tolerant output tracking control of 4WS4WD road vehicles,” *IEEE Trans. Intell. Transp. Syst.*, vol. 14, no. 1, pp. 169–179, Mar. 2013.

- [15] C. Chen, Y. Jia, J. Du, and F. Yu, "Lane keeping control for autonomous 4WS4WD vehicles subject to wheel slip constraint," in *Proc. Amer. Control Conf.*, Jun. 2012, pp. 6515–6520.
- [16] R. Potluri and A. K. Singh, "Path-tracking control of an autonomous 4WS4WD electric vehicle using driving motors' dynamics," in *Proc. 7th IEEE ICIS*, Chennai, India, Aug. 2012, pp. 1–6.
- [17] R. Potluri and A. K. Singh, "Path-tracking control of an autonomous 4WS4WD electric vehicle using its natural feedback loops," in *Proc. IEEE Multi-Conf. Syst. Control (IEEE MSC)*, Hyderabad, India, Aug. 2013, pp. 394–400.
- [18] Z. Gao and R. R. Rhinehart, "Theory vs. practice: The challenges from industry," in *Proc. Amer. Control Conf.*, Boston, MA, USA, Jun./Jul. 2004, pp. 1341–1349.
- [19] "Andrzej Banaszuk [People in Control]," *IEEE Control Syst.*, vol. 32, no. 3, pp. 27–31, Jun. 2012.
- [20] A. Alleyne, "A comparison of alternative intervention strategies for unintended roadway departure (URD) control," *Vehicle Syst. Dyn., Int. J. Vehicle Mech. Mobility*, vol. 27, no. 3, pp. 157–186, Jul. 1997.
- [21] U. Kiencke and L. Nielsen, *Automotive Control Systems: For Engine, Driveline, and Vehicle*, 2nd ed. New York, NY, USA: Springer-Verlag, 2005.
- [22] H. A. Toliyat and G. B. Kliman, Eds., "Electronic motors," in *Handbook of Electric Motors*, 2nd ed. Boca Raton, FL, USA: CRC Press, 2004.
- [23] T. Umeno and Y. Hori, "Robust speed control of DC servomotors using modern two degrees-of-freedom controller design," *IEEE Trans. Ind. Electron.*, vol. 38, no. 5, pp. 363–368, Oct. 1991.
- [24] J. Ackermann, *Robust Control: The Parameter Space Approach*. New York, NY, USA: Springer-Verlag, 2002.
- [25] C. P. Connette, C. Parlitz, B. Graf, M. Häggle, and A. Verl, "The mobility concept of Care-O-bot 3," in *Proc. 39th Int. Symp. Robot. (ISR)*, vol. 15, 2008, p. 17.
- [26] J. Ploeg, A. C. M. van der Knaap, and D. J. Verburg, "ATS/AGV-design, implementation and evaluation of a high performance AGV," in *Proc. IEEE Intell. Veh. Symp.*, vol. 1, Jun. 2002, pp. 127–134.
- [27] R. Leenen, "Motion control design for a 4ws and 4wd overactuated vehicle," M.S. thesis, Dept. Mech. Eng., Eindhoven Univ. Technol., Eindhoven, The Netherlands, 2004.
- [28] H. K. Khalil, *Nonlinear Systems*, 3rd ed. Englewood Cliffs, NJ, USA: Prentice-Hall, 2002.
- [29] T. J. Gordon, "An integrated strategy for the control of a full vehicle active suspension system," *Vehicle Syst. Dyn., Int. J. Vehicle Mech. Mobility*, vol. 25, no. S1, pp. 229–242, 1996.